Solar minimum exospheric neutral density near the subsolar magnetopause estimated from the XMM soft X-ray observations on 12 November 2008

Jaewoong Jung, Hyunju K. Connor, Jennifer A. Carter, Dimitra Koutroumpa, Claudio Pagani, K. D. Kuntz

JGR Space Physics

RESEARCH ARTICLE
10.1029/2021JA029676

Key Points:

- From 11 years of X-ray Multimirror Mission-Newton X-ray observations, we identified 193 intervals that can be used to estimate the exospheric neutral density
- We derived a solar minimum exospheric neutral density from the 12 November 2008 event using a global MagnetoHydroDynamics model and a simplified exosphere model
- The density estimate is 36.8 cm^{-3} near the subsolar magnetopause and is likely a lower-limit value

Supporting Information:

Supporting Information may be found in the online version of this article.

Correspondence to:

J. Jung,
jjung11@alaska.edu

Citation:

Jung, J., Connor, H. K., Carter, J. A., Koutroumpa, D., Pagani, C., & Kuntz, K. D. (2022). Solar minimum exospheric neutral density near the subsolar magnetopause estimated from the XMM soft X-ray observations on 12 November 2008. *Journal of Geophysical Research: Space Physics*, *127*, e2021JA029676. https://doi.org/10.1029/2021JA029676

Received 21 JUN 2021
Accepted 25 FEB 2022

Author Contributions:

Conceptualization: H. K. Connor, J. A. Carter
Data curation: J. Jung
Formal analysis: J. Jung, H. K. Connor
Funding acquisition: H. K. Connor
Investigation: J. Jung, H. K. Connor
Methodology: J. Jung, H. K. Connor, J. A. Carter, D. Koutroumpa
Project Administration: H. K. Connor
Resources: J. Jung, H. K. Connor, J. A. Carter
Software: J. Jung, H. K. Connor, J. A. Carter, C. Pagani
Supervision: J. Jung, H. K. Connor, J. A. Carter
Validation: J. Jung, H. K. Connor, J. A. Carter, D. Koutroumpa, K. D. Kuntz

Solar Minimum Exospheric Neutral Density Near the Subsolar Magnetopause Estimated From the XMM Soft X-Ray Observations on 12 November 2008

J. Jung[1], H. K. Connor[1,2], J. A. Carter[3], D. Koutroumpa[4], C. Pagani[3], and K. D. Kuntz[5]

[1]Geophysical Institute, University of Alaska Fairbanks, Fairbanks, AK, USA, [2]NASA Goddard Space Flight Center, Greenbelt, MD, USA, [3]University of Leicester, Leicester, UK, [4]LATMOS-IPSL, CNRS, UVSQ Paris-Saclay, Sorbonne Université, Guyancourt, France, [5]The Henry A. Rowland Department of Physics and Astronomy, Johns Hopkins University, Baltimore, MD, USA

Abstract The Earth's magnetosheath and cusps emit soft X-rays due to the charge exchange between highly charged solar wind ions and exospheric hydrogen atoms. The Lunar Environment Heliospheric X-ray Imager and Solar wind Magnetosphere Ionosphere Link Explorer missions are scheduled to image the Earth's dayside magnetosphere system in soft X-rays to investigate global-scale magnetopause reconnection modes under varying solar wind conditions. The exospheric neutral hydrogen density distribution, especially the value of this density at the subsolar magnetopause is of particular interest for understanding X-ray emissions near this boundary. This paper estimates the exospheric density during solar minimum using the X-ray Multimirror Mission (XMM) astrophysics observatory. We selected an event on 12 November 2008 from the XMM data archive, which detects soft X-rays of magnetosheath origin while solar wind and interplanetary magnetic field conditions are relatively constant. During the event the location of the magnetopause was measured in situ by the THEMIS mission, thus the location of the solar wind ions responsible for the magnetosheath emission is well constrained by observation. We estimated the exospheric density using the Open Geospace Global Circulation Model (OpenGGCM) and a spherically symmetric exosphere model. The ratio of the magnetosheath plasma flux between the OpenGGCM model and the THEMIS, was nearly 1, which means the magnetohydrodynamic model reasonably reproduces the magnetosheath plasma conditions. The OpenGGCM magnetosheath parameters were used to deconvolve soft X-rays of exospheric origin from the XMM signal. The lower-limit of the exospheric density of this solar minimum event is 36.8 ± 11.7 cm^{-3} at 10 R_E subsolar location.

1. Introduction

Understanding when, where, and how the magnetopause reconnection occurs is one of the most important topics in space physics. Tracking magnetopause reconnection on a global scale has been particularly challenging due to the lack of possibly simultaneous observations covering wide spatial regions of the magnetopause. Recently, soft X-ray imaging of the Earth's dayside system has been suggested as an innovative way to visualize the dayside magnetopause motion and thus infer the dayside reconnection mode (Connor et al., 2021).

A small portion of the solar wind plasma consists of highly charged ions, like O^{7+} and O^{8+}. The Earth's exosphere is the outermost layer of the atmosphere composed of mostly hydrogen atoms. When the ion collides with an exospheric neutral, the ion can capture an electron from the neutral atom. In the relaxation stage, soft X-rays are emitted:

$$S^{q+} + B \rightarrow S^{(q-1)+*} + B^{+} \quad (1)$$

$$S^{(q-1)+*} \rightarrow S^{(q-1)+} + h\nu \quad (2)$$

where S is a solar wind origin ion, q is its charge state, * represents an excited state, and B is an exospheric neutral. This process is called Solar Wind Charge Exchange (SWCX) (Sibeck et al., 2018 and references therein).

After the first discovery of cometary X-ray emission (Lisse et al., 1996), Cravens (1997) suggested the SWCX process as a possible mechanism of such X-rays. Soon, Cravens et al. (2001) reported that the diffuse background variation observed by the low-Earth orbit ROSAT astrophysics mission tracked variations in solar wind flux quite

Visualization: J. Jung, H. K. Connor
Writing – original draft: J. Jung, H. K. Connor
Writing – review & editing: J. Jung, H. K. Connor, J. A. Carter, D. Koutroumpa, C. Pagani, K. D. Kuntz

well, implying that the Earth's outer atmosphere is a strong soft X-ray emitter. Subsequently, other astrophysics missions like X-ray Multimirror Mission (XMM)-Newton (Jansen et al., 2001; hereafter XMM), Suzaku (Mitsuda et al., 2007), and Chandra (Weisskopf et al., 2000) reported the detection of near-Earth soft X-ray emissions (Kuntz & Snowden, 2008; see also; Carter, Sembay, & Read, 2010; Ishikawa et al., 2013), which strongly motivates the space science community to study the solar wind—magnetosphere interaction through these signals. For this purpose, space missions such as Cusp Plasma Imaging Detector (CuPID; http://sites.bu.edu/cupid) Cubesat observatory, Lunar Environment heliospheric X-ray Imager (LEXI; http://sites.bu.edu/lexi), and the Solar wind—Magnetosphere —Ionosphere Link Explorer (SMILE; Branduardi-Raymont et al., 2018) have been planned and will be launched in the next few years.

The Earth's magnetosheath and cusps strongly emit in soft X-rays because the magnetosheath has a dense population of high-charge-state solar wind ions and a non-negligible population of exospheric hydrogens and because the cusps have dense populations of exospheric hydrogens and non-negligible density of high-charge-state ions (Connor et al., 2021; Sibeck et al., 2018). The SWCX emission rate is controlled by three factors: the neutral density, plasma ion density, and relative velocity between neutrals and ions (Connor & Carter, 2019; hereafter CC2019). While the plasma density, velocity, and temperature in the magnetosphere are well understood by the heliophysics missions like Cluster, THEMIS, and MMS (Dimmock & Nykyri, 2013), the neutral density in the magnetosheath is poorly understood due to the severe lack of the exospheric observations above an altitude of 7 Earth radii (R_E). Under $7R_E$, the Geocoronal Lyman-α observations have been a widely used data set for the neutral density studies (Bailey & Gruntman, 2011; Baliukin et al., 2019; Zoennchen, Bailey, et al., 2011; Zoennchen, Nass, & Fahr, 2013, 2015; Zoennchen, Nass, Fahr, & Goldstein, 2017; Østgaard et al., 2003). However, above 7 R_E interplanetary Lyman-α background overwhelms the geocoronal emission. Additionally, the dayside geocorona data are often contaminated by direct sunlight due to the close proximity of the instrument's line of sight (LOS) to the Sun. Recently, CC2019 suggested the SWCX observed by the XMM satellite as an alternative source of data for the study of the exospheric neutral density in the dayside magnetosheath.

Energetic neutral atoms (ENAs) have also been used to study the neutral density in the outer exosphere, for example, using the two ENA cameras on the Interstellar Boundary EXplorer (IBEX; Funsten et al., 2009; Fuselier et al., 2009; McComas et al., 2009). ENAs are produced when solar wind proton steals electrons from the neutral atoms in the Earth's exosphere. Fuselier et al. (2010) estimated a neutral density of 4–11 cm^{-3} at the 10 R_E subsolar point by analyzing several solar minimum events of IBEX with a simplified magnetosheath model. Fuselier et al. (2020) conducted a similar study for a solar maximum event but with an improved magnetosheath model, and obtained the neutral density of 11–17 cm^{-3} at the 10 R_E subsolar location.

In this paper, we selected one event from the XMM database that occurred during solar minimum and estimated a neutral density at the 10 R_E subsolar location, considering that a typical subsolar magnetopause is located at about 10 R_E (Kivelson & Bagenal, 2014). Finally, we compared our solar minimum exospheric density with the solar maximum density of CC2019 and with the neutral density in other studies.

This paper is structured as follows. In Section 2, we introduce the data and models used in this study. In Section 3, we explain our methodology for deriving the exospheric density from the XMM observations. In Section 4, we discuss our event selection process using the 11 years of XMM soft X-ray data. In Section 5, we present our case study of the 12 November 2008 event and estimate a neutral density during solar minimum. In Section 6, we compare our neutral density result with those in previous literature. Finally, in Section 7 we summarize our study.

2. Data and Model

2.1. XMM Data

The XMM observatory (Jansen et al., 2001) is an observatory-class mission launched by the European Space Agency in 1999 to investigate the astrophysical X-ray sky. XMM has an orbital inclination of ∼−40°. The apogee is 114,000 km, and the perigee is 7,000 km. The orbital period is ∼48 hr. Onboard XMM, there are three imaging cameras that use X-ray CCD detectors at the focal plane, which make up the suite of instruments known as the European Photon Imaging Camera (EPIC). Two of the cameras are front-illuminated metal oxide semiconductor (MOS) CCD arrays (Turner et al., 2001) and the other camera uses back-illuminated PN CCD arrays called PN camera (Strüder et al., 2001). As XMM was designed to investigate distant X-ray astrophysical sources, many of which are extragalactic, the telescope fields of view (FOV) is narrow: $33' \times 33'$ for MOS (9.2×10^{-5} sr) and

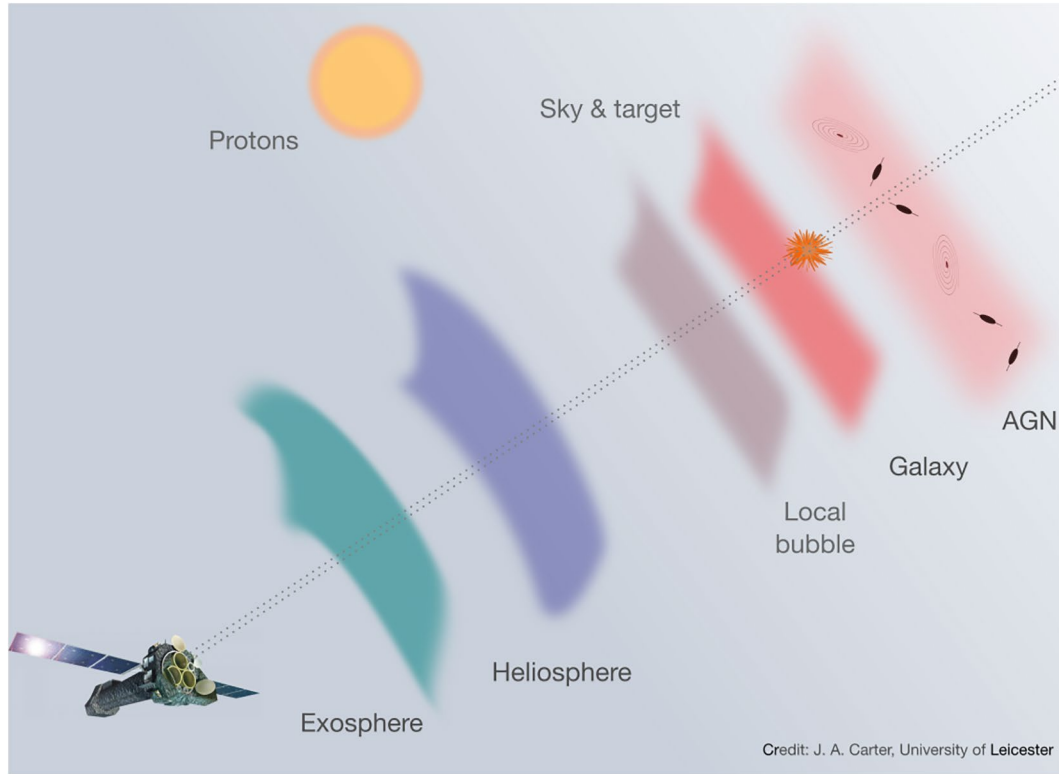

Figure 1. Various X-ray signals and the soft protons that create false counts in X-ray Multimirror Mission X-ray cameras.

27.5′ × 27.5′ for PN. XMM has a restricted view geometry due to the constraints imposed on the orientation of its solar panels. Depending on the geometry of the orbit and pointing requirement at the time of a particular observation, the telescope's LOS may pass through the Earth's dayside magnetosheath, which would result in the imposition of a foreground SWCX signal on the signal from the background X-ray sky, as illustrated in Figure 1.

Figure 1 summarizes various X-ray signals and the soft protons that create false counts in XMM X-ray cameras. The raw XMM-measured signal includes different components, namely, astrophysical point sources, the instrumental background, the sky background, the heliospheric background, the near-Earth SWCX, and at times, soft proton contamination. We need to identify the SWCX component for estimating the Earth's exospheric density. Section 5.1 explains the details of the background removal process.

We downloaded Original Data Files (ODFs) from the XMM Science Archive (XSA) and processed the data using the XMM Science Analysis System (SAS) software package version 18.0.0 (de la Calle, 2021), provided at the XMM data analysis web page: https://www.cosmos.esa.int/web/xmm-newton/sas. We used the MOS full-frame observation data, since some SAS commands needed in this study can be applied only to the full-frame mode data. In this paper, the XMM observations between revolutions 21 and 1990 are used, which corresponds to the period from January 2000 to October 2010.

2.2. OpenGGCM Model

XMM can detect soft X-rays created in the magnetosheath as a result of the interaction between solar wind origin ions and exospheric neutrals. To derive an exospheric density, the plasma contributions should be disentangled from the XMM SWCX observations. We used the OpenGGCM global magnetosphere-ionosphere Magneto-HydroDynamics (MHD) model to reproduce the magnetosheath plasma condition during the XMM observation period. OpenGGCM calculates the plasma density, velocity, temperature, and electromagnetic fields near the Earth's magnetosphere using the Solar Wind (SW) and interplanetary magnetic field (IMF) as inputs. In this paper, a stand-alone OpenGGCM model is used with the NASA WIND spacecraft data. More details and applications of the OpenGGCM model can be found in Raeder et al. (2001, 2008); see also Connor et al.

(2012, 2014, 2015, 2016, 2021), Cramer et al. (2017), Ferdousi and Raeder (2016), Ferdousi et al. (2021), Jensen et al. (2017), Kavosi et al. (2018), Oliveira and Raeder (2015), and Shi et al. (2017).

To validate the OpenGGCM simulation result, we compared it with the THEMIS B in situ data. We used electrostatic analyzer (ESA; McFadden et al., 2008) and fluxgate magnetometer (FGM; Auster et al., 2008) data. The ESA data used in this paper have a time resolution of few minutes (except for the plasma density, which has a 3-s resolution), and FGM data have a time resolution of 3 s. We calculated the running average of the FGM and ESA data every 10 min using a 10-min window.

3. Methodology

This study improves the method of CC2019 by considering soft X-ray signals in the 0.4–1.0 keV energy band. CC2019 considered only a few oxygen lines in the 0.5–0.7 keV band. Thus, their soft X-ray signals and subsequently, their neutral density estimates tended to be sensitive to the highly variable oxygen abundance in the solar wind, as reported in Kuntz et al. (2015). On the other hand, the 0.4–1.0 keV energy band includes various SWCX lines (Sibeck et al., 2018). The soft X-ray signals in this wide band are dependent on the sum of the high-charge-state ions in the solar wind. Thus, our neutral density estimate is less sensitive to individual ion abundance.

First, we assumed that the neutral density is spherically symmetric and inversely proportional to the distance cubed, as in Cravens et al. (2001):

$$N_N = N_0 \left(\frac{10 R_E}{R} \right)^3 \quad \left[\mathrm{cm}^{-3}\right] \tag{3}$$

where N_0 is a neutral hydrogen density at the 10 R_E subsolar point, that is, at a typical subsolar magnetopause location (this density is hereafter referred to as a characteristic neutral density), and R is the radial distance from the Earth's center in R_E.

Second, we calculated a soft X-ray emission rate for each SWCX spectral line j (R_j) using the following equation (Kuntz, 2019):

$$R_j = E_j \int N_N N_{sq} v_{eff} \sigma_{sq} Y_j \frac{ds}{4\pi} \quad \left[\mathrm{eV\ cm^{-2}\ s^{-1}\ sr^{-1}}\right] \tag{4}$$

where E_j is the emission line energy of transition j in eV, N_N is the exospheric neutral density in cm^{-3}, N_{sq} is the number density of a solar wind ion of species s in cm^{-3}, q(S^{q+}) is the charge state of N_{sq}, v_{eff} is the relative velocity of the ion and the neutral (also called the effective velocity) in km/s, σ_{sq} is the cross section of the interaction between S^{q+} and hydrogen in cm^2, Y_j is the photon yield for the transition of $S^{(q-1)+}$ in number of photons, and ds is a spatial step for the integration along the LOS.

Third, we defined the potential reaction rate (Q), the part that we can calculate from the parameters provided by the OpenGGCM MHD model, as follows:

$$Q = \int \frac{N_N}{N_0} N_p v_{eff} ds = \int \left(\frac{10 R_E}{R} \right)^3 N_p v_{eff} ds \quad \left[\mathrm{cm^{-1}s^{-1}}\right] \tag{5}$$

$$v_{eff} = \sqrt{v_p^2 + 3kT/m} \quad [km/s] \tag{6}$$

where m, N_p, v_p, and T are the proton mass, density, drift velocity, and temperature, respectively, and k is the Boltzmann constant. The effective velocity (v_{eff}) is the relative velocity between the plasma and a neutral atom. However, as the velocity of the neutral atom is far smaller than the plasma velocity, it is sufficient to only consider the plasma velocity. Then, Equation 4 becomes

$$R_j = \frac{1}{4\pi} Q N_0 E_j \frac{N_{sq}}{N_p} \sigma_{sq} Y_j \tag{7}$$

Here, we assumed that the densities ratio of high-charge-state ion to proton (N_{sq}/N_p) stays constant along the LOS.

Fourth, we converted the emission rate R_j to a simulated soft X-ray count rate (CR_{MHD}) based on the XMM instrument properties:

$$CR_{MHD} = \sum_{E_j \in E} \frac{\Omega A_j}{E_j} R_j = \frac{1}{4\pi} \beta \Omega Q N_0 \quad [cts/s] \tag{8}$$

where Ω is the XMM field-of-view in sr, and A_j is the effective area of XMM in cm^2 at the X-ray energy E_j. The summation is done over all the spectral lines of energy E_j inside the energy band of our interest (0.4–1.0 keV). The effective scale factor (β) considers the charge exchange mechanism of all the individual SWCX lines in our energy band:

$$\beta = \sum_{E_j \in E} A_j \frac{N_{sq}}{N_p} \sigma_{sq} Y_j \quad [\mathrm{cm}^4] \tag{9}$$

CC2019 used an effective scale factor α that considered only a weight-averaged emission line at 590.5 eV because they focused on the X-ray emission in a narrow energy band (0.5–0.7 keV). Since O^{7+} and O^{8+} are the main contributors to this energy band (Kuntz et al., 2015), the X-ray count rates become very sensitive to the oxygen abundance in solar wind, which may break the assumption of the constant oxygen-to-hydrogen ratio used in CC2019. To avoid such a problem, we focused on a wider energy band (0.4–1.0 keV) that includes emission lines from various charge-state solar wind ions (e.g., C^{6+}, N^{6+}, N^{7+}, Ne^{9+}, S^{10+}, O^{7+}, and O^{8+}). An example of a SWCX spectrum in the range of 0.1–1 keV can be found in Figure 15 of Sibeck et al. (2018). The total abundance of all the SWCX source ions in solar wind is expected to be more stationary than the abundance of oxygen itself in the solar wind, thus better satisfying our assumption and subsequently providing a more accurate neutral density estimate. Thus, the effective scale factor β is better suited to our wide-band X-ray study than α.

The effective area A_j can be obtained from the XMM Auxiliary Response File (ARF). The ARF file contains a table that includes the effective area information at each energy level. The effective areas of the XMM MOS cameras are fully described by the instrument calibration teams, and the link to these data is listed in the Acknowledgments. The thin filter was used for this XMM observation. For the densities ratio of highly charged ion to proton (N_{sq}/N_p), the CX cross section (σ_{sq}), and the photon yield (Y_j), we used the data of Koutroumpa et al. (2006) (assuming a slow solar wind). The resulting β for 12 November 2008 event is 1.53×10^{-16} cm^4.

Finally, assuming that Equation 3 is a good representation of our exospheric density distribution, the modeled count rate (CR_{MHD}) should be equal to the SWCX count rates observed by XMM (CR_{SWCX}), with $CR_{MHD} = CR_{SWCX}$. Using Equation 8, the characteristic density N_0, that is, the exospheric density at the 10 R_E subsolar point, becomes:

$$N_0 = \frac{4\pi}{\beta \Omega Q} CR_{SWCX} \tag{10}$$

4. Event Selection

Carter et al. (2011) selected 103 XMM soft X-ray observations that showed temporal variability in the 0.5–0.7 keV energy band compared to the 2.5–5.0 keV continuum band. These observations are considered the near-Earth SWCX events because the astronomical soft X-rays are almost constant within a time scale of several hours to a few days. CC2019 selected two of these observations and derived solar maximum neutral densities. However, the event selection criteria in Carter et al. (2011) tends to find cases during dynamic SW/IMF conditions, which may complicate the reproduction of the magnetosheath conditions, and thus the calculation of the plasma contribution to the near-Earth soft X-ray emissions. To avoid such a problem, we searched 11 years of XMM observations and created a new list of XMM events suited to our exospheric density studies. We describe below the four steps we took to select the new event.

First, we selected the potential near-Earth SWCX events by searching for the times when XMM looks through the dayside magnetosheath, where strong soft X-ray emissions are expected, during relatively constant solar wind and IMF conditions. We avoided the dynamic upstream conditions because a global MHD model may have difficulty reproducing a complex solar wind—magnetosphere interaction. Figure 2a shows examples of selected (left) and not selected (right) XMM events under our selection process. The orange lines represent the bow shock locations at the start (solid) and at the end (dashed) of the XMM observation time, calculated from Jeřáb et al. (2005) using

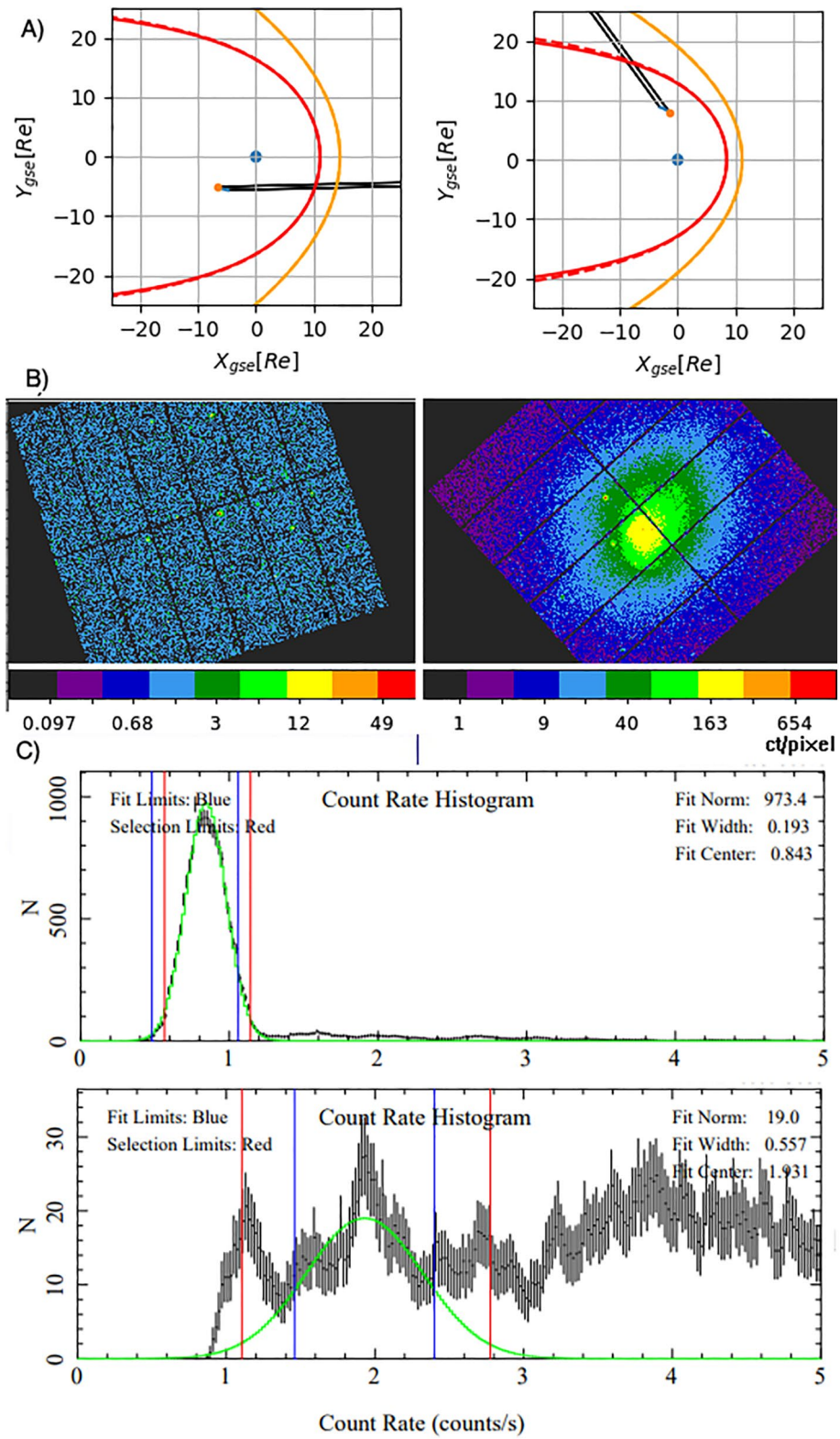

Figure 2. Example of the X-ray Multimirror Mission (XMM) observation selection process: (a) Line of sight (LOS) direction inspection. We selected the observation on the left panel and discarded the observation on the right panel, because stronger X-ray emissions are expected from the dayside magnetosheath, (b) two images made from the XMM PN data. The image on the right shows an extended point source that almost fills the telescopic fields of view (FOV), and therefore, this observation was excluded from further analysis. The unit of the X-ray images is counts/pixel (The XMM MOS pixel size is $1.1'' \times 1.1''$.), (c) Soft proton flaring check. We selected the observation represented by the upper panel and discarded the observation on the lower panel, as described in the main text.

the NASA WIND spacecraft data. Similarly, red lines indicate the magnetopause locations at the start (solid) and at the end (dashed) of the XMM observation time, calculated from the model of Shue et al. (1998). The blue and black lines represent the XMM orbit and the LOS direction during the observation period, respectively. We selected the event on the left panel of Figure 2a because the dayside boundaries were relatively stationary during the observation period and because XMM looked through the dayside magnetosheath.

Second, we removed events where bright and particularly extended X-ray sources are found in the FOV. Figure 2b shows the XMM examples selected (left) and not selected (right) in this process. The near-Earth SWCX signals were derived from the background signals; for example, from the blue region on the left panel of Figure 2b. If the X-ray sources are very bright and/or extended as, for example, on the right panel of Figure 2b, photons from the astrophysical source may be accidently incorporated into the background signal even after filtering for astrophysical sources. We visually inspected the images from the XMM observations for the presence of bright sources, a technique also applied in Carter et al. (2011). Any observations with astronomical sources larger than 500 arcsecs were excluded from further analysis.

Third, we excluded the XMM events that were badly contaminated by soft proton flaring. Energetic protons of a few hundred keV, called soft protons, can reach the XMM camera detectors and falsely create a signal at the detector plane. At times, the soft proton signals are very strong and dominate other X-ray sources. This is known as soft proton flaring (Lumb et al., 2002; Walsh et al., 2014) and has to be removed from our event selection. Using the HEASARC XMM trend data, we compared two light curves for a band between 2.5 and 12 keV, where no other X-ray signals except soft protons and an instrumental background are expected due to the very high energy range. The in-FOV light curve in this energy band is affected by both the incoming soft proton flaring and the instrumental background, while the out-of-FOV light curve was only affected by the instrumental background. Therefore, by comparing these two light curves, we can determine when the soft proton flaring occurred (Carter & Sembay, 2008). Additionally, we also utilized count rate histograms for the soft flaring check. The top and bottom panels of Figure 2c show examples of count rate histograms with and without soft proton flaring, respectively. In the case of severe soft proton flaring, the count rate histogram (black) does not match Gaussian profile (green). We excluded observations heavily affected by soft proton flaring.

Finally, we selected the XMM observations when a solar wind monitor like ACE and WIND provided good-quality solar wind/IMF data and when a heliophysics satellite like Cluster, Geotail, and THEMIS provided in situ magnetosheath plasma observations. For our purposes, good-quality solar wind/IMF data means time intervals with relatively constant density, velocity, and IMF B_Z. The solar wind and IMF data were used as inputs for the OpenGGCM model, and the in situ magnetosheath plasma data were used to validate the model results.

From the XMM observations between the years 2000 and 2010, we found 193 potential SWCX events that are well suited for our density derivation techniques. In this study, we selected an event on 12 November 2008 for estimating a solar minimum exospheric density (XMM observation number 0551860501). We will use the rest of the events in the list for our future neutral density study.

5. Case Study of the 12 November 2008 Event

5.1. Extraction of the Near-Earth SWCX Counts

As discussed in Section 2.1, the raw XMM data includes soft proton contamination, astrophysical point sources, the instrumental background, the sky background, the heliospheric background, and near-Earth SWCX signals. In this section, we follow the general procedures used in the astrophysics community to estimate the contribution of background and noise components and thus, derive the terrestrial signals from the raw XMM observation on 12 November 2008.

First, we extracted the total XMM background rate by removing the soft proton contamination period and the signal from the astrophysical point sources in the XMM data. Although we removed the periods of soft proton flaring, there could be variations on the longer timescales that were missed in our method; that is, some residual soft proton flaring may remain in our data but will not have a time variation on the scales of interest. To remove this additional contamination period, we calibrated event files from the original data files using the SAS subroutine *emproc*. Then, we created a good-time-interval (GTI). The GTI file contains a record of the the times when there was no proton flaring. We applied the GTI files to the event file to remove the contaminated time intervals.

It is common for about 36% of the XMM time to be lost to soft protons (Kuntz & Snowden, 2008). After applying the GTI file, we removed astrophysical point sources from the FOV. Generally, we followed the method of Carter et al. (2011), except that we used *edetect_chain* to detect the point sources. We applied a 35-arcsec extraction radius at each point source. After the automatic astrophysical point source removal process, we visually checked relevant images generated from the cleaned XMM data, after which we applied an additional source removal of a 500-arcsec radius about the telescope boresight to ensure that any bright on-axis astrophysical source was largely eliminated. From this first step, we estimated a total XMM background count of the 12 November 2008 event at 4.3×10^3 counts for 3.3 hr of exposure time.

Second, we estimated the instrumental background caused by both the high-energy particles that produce charge directly in the CCDs and the particle-induced X-rays generated inside the camera. For example, galactic cosmic ray (GCR) particles can interact with the detector to produce secondaries that generate background signal. EPIC instrumental background files can be obtained with the filter wheel in a closed position (Kuntz & Snowden, 2008). Filter Wheel Closed (FWC) data, that is, the data that is dominated by the instrumental background and can be used to model the internal instrumental background, is available through the XMM Science Operation Centre from the EPIC Background Analysis web pages. Since SAS v.16, the task *evqpb* has been available to generate a tailored FWC event file that corresponds to an observation. As XMM science observation and FWC data are not recorded simultaneously, they may have different intensities of instrumental backgrounds. We renormalized the instrumental background of the FWC data to obtain the background of our observation by following the methods of De Luca and Molendi (2004) and Carter et al. (2011). We calculated the scaling factor by comparing our observation with the FWC data in a high energy band (7.5–9 keV) where, for the period free of soft proton flaring, the contribution is believed to be entirely from the instrumental background. We obtained the instrumental background of our observations by multiplying the FWC background by the scale factor. The total instrumental background count for the 12 November 2008 event is 2.0×10^3 counts.

Third, we estimated the sky background. We utilized a HEASARC X-ray background command line tool (https://heasarc.gsfc.nasa.gov/Tools/xraybg_help.html\#command) to get the ROSAT all-sky survey data (Snowden et al., 1997) for the given galactic coordinate. Following Galeazzi et al. (2007), we modeled the ROSAT diffuse spectrum with three components. Two of them are unabsorbed and absorbed plasma components that represent X-ray emissions from the diffuse local interstellar and more distant galactic halo components, respectively. We used the APEC (Smith et al., 2001) model within *XSPEC* (https://heasarc.gsfc.nasa.gov/xanadu/xspec/) to calculate these plasma components. The last component is the absorbed power law that represents the unresolved extragalactic X-ray background. We calculated the last component using *wabs* model (Morrison & McCammon, 1983) by considering the absorption by the neutral hydrogen in the Galaxy along the LOS of our XMM event. We converted ROSAT to the XMM count rates through an algorithm provided by the NASA HEASARC team that was adapted for our local use. A constant sky background was expected throughout our event because the satellite pointing was fixed and because our event was only ∼3.3 hr long, much shorter than the time scale of the sky background variation. As we will note later, the sky background obtained from the ROSAT data may contain some fraction that originates from the heliosphere. The total sky background for the 12 November 2008 event is 1.5×10^3 counts.

Fourth, we subtracted a heliospheric background component. SWCX is also produced within the heliosphere via a charge exchange interaction between interplanetary neutrals and solar wind plasma. This signal depends on the neutral and plasma density distributions along the instrument's LOS at the time of the observation (Koutroumpa et al., 2006). The heliospheric hydrogen and helium distributions were calculated as in Koutroumpa et al. (2006), based on the "hot model" simulations of Lallement et al. (1985) and Dalaudier et al. (1984), respectively. The distributions were adjusted to the solar activity corresponding to late 2008. By assuming a solar wind flux of 2.0×10^8 cm^{-2} s^{-1}, we obtained the total heliospheric signal of the 12 November 2008 event at 7.7×10^2 counts. Koutroumpa et al. (2019), Bzowski et al. (2013), Machol et al. (2019), and McMullin et al. (2004) provides additional details on heliospheric signal calculation for interested readers.

Finally, we obtained the near-Earth SWCX of our event by subtracting the instrumental, sky, and heliospheric backgrounds from the total XMM background counts. The resulting terrestrial SWCX counts is $(1.0 \pm 0.18) \times 10^2$ counts for the 3.3-hr observation period on 12 November 2008. Table 1 summarizes all the background components.

Table 1
Summary of the Soft X-Ray Background Counts for the 12 November 2008 Event, in the Energy Band of 0.4–1.0 keV

Component	Counts	Contribution (%)
Total (C_{bgd})	4.3×10^3	100
Instrumental (C_{inst})	2.0×10^3	46.6
Astronomical (C_{sky})	1.5×10^3	33.4
Heliospheric (C_{helio})	7.7×10^2	17.7
SWCX (C_{SWCX})	1.0×10^2	2.3

The near-earth SWCX count is only 2.3% of the total X-ray background count. This may be a concern of heliophysics readers who have dealt with the data from signal-abundant near-Earth space environments. However, for X-ray background astronomers, weak X-ray signals are common. They have developed rigorous techniques to understand our universes in X-rays and have published numerous studies on X-ray backgrounds, including near-Earth SWCX signals (Carter et al., 2010; Cravens, 1997; Cravens et al., 2001; Ishikawa et al., 2013; Kuntz & Snowden, 2008; Snowden et al., 1997; Whittaker et al., 2016). Although not documented here, we have compared our background counts to those of other astronomers who used more sophisticated background removal techniques. Our background signals are comparable to or higher than their values. We took higher background signals obtained from our techniques and subsequently underestimated the SWCX signals because we are interested in the lower-end exospheric density, an important quantity for the SMILE and LEXI teams to understand the minimum SWCX signals and thus prepare their mission accordingly. We also performed a spectral analysis of the entire event interval using the X-ray fitting software Xspec to double check if our XMM observation included SWCX signals. We found that our fitting results were significantly improved by the addition of the SWCX emission lines. Finally, we performed the same background removal processes for an XMM event that was expected to see no near-Earth SWCX signal. We found that the residual soft X-ray count is nearly zero or 0.03% of the total X-ray background count, demonstrating the robustness of our background removal techniques. Therefore, to the best of our knowledge on the X-ray backgrounds and the available background removal techniques, XMM did observe near-Earth signals, and our SWCX count is considered a minimum value.

5.2. Neutral Density Estimation

We derived an exospheric neutral density from the 12 November 2008 event. About 3.3 hr of soft X-ray data (03:43–07:03 UT) were available from the EPIC MOS observations. Figure 3 summarizes the orbital and observational details of the spacecraft observations, as well as the IMF and solar wind conditions during the period of interest. Figure 3a displays the XMM orbit (blue line), its LOS direction (black line), the THEMIS-B orbit (green line), the magnetopause location (red line), and the bow shock location (yellow line) projected on the Geocentric Solar Ecliptic (GSE) XY (left) and XZ (right) planes during the observation period. The orange/red dots present the starting locations of XMM/THEMIS B for this event, respectively. Figure 3b shows, from top to bottom, the IMF, solar wind velocity, number density, plasma pressure ($P = nkT$), and solar wind proton flux ($n_{sw}V_{sw,x}$). The green and gray shaded areas indicate intervals of XMM near-Earth SWCX observation and the THEMIS-B magnetosheath observation, respectively. We used the WIND plasma and magnetic field observations, downloaded from the NASA CDAWeb. WIND was located at 239.4 R_E sunward, and its data were time-shifted by 1.24 hr to consider the solar wind propagation from WIND to a subsolar bow shock using the minimum variance method explained in Raeder et al. (2008) and the references therein. The magnetic field observed from the Magnetic Field Investigation (MFI; Lepping et al., 1995) instrument had a 1-min resolution, and the plasma data from the Solar Wind Experiment (SWE; Ogilvie et al., 1995) instrument had a 92-s resolution. Both the magnetic field and the solar wind data were adjusted to have a 1-min resolution using a linear interpolation method before they were submitted to the OpenGGCM model.

XMM moved from (−0.88, 8.68, −9.96) to (−3.09, 7.26, −13.03)R_E in the GSE coordinates, and its LOS direction was fixed at (0.28, 0.63, and 0.73) in the GSE coordinates that used the XMM location as the origin. During the XMM observation, THEMIS-B crossed the dawnside magnetosheath (from [−6.11, −20.55, −2.61] to [−5.05, −25.27, −3.07]R_E), providing not only the plasma conditions in the magnetosheath but also the locations of the magnetopause and the bow shock. We used these THEMIS-B data for model validation and the model-induced error analysis in our density estimates. Throughout this short observation, the solar wind condition and the IMF magnitude did not show a drastic change. The maximum-to-minimum difference in the solar wind density was 2.19 cm^{-3} (with a maximum of 5.85 cm^{-3} and a minimum of 3.64 cm^{-3}), and that of the IMF B_Z was 3.07 nT (from 0.66 to 3.73 nT) We simulated the 12 November 2008 event using the solar wind and IMF conditions in Figure 3b as inputs for OpenGGCM.

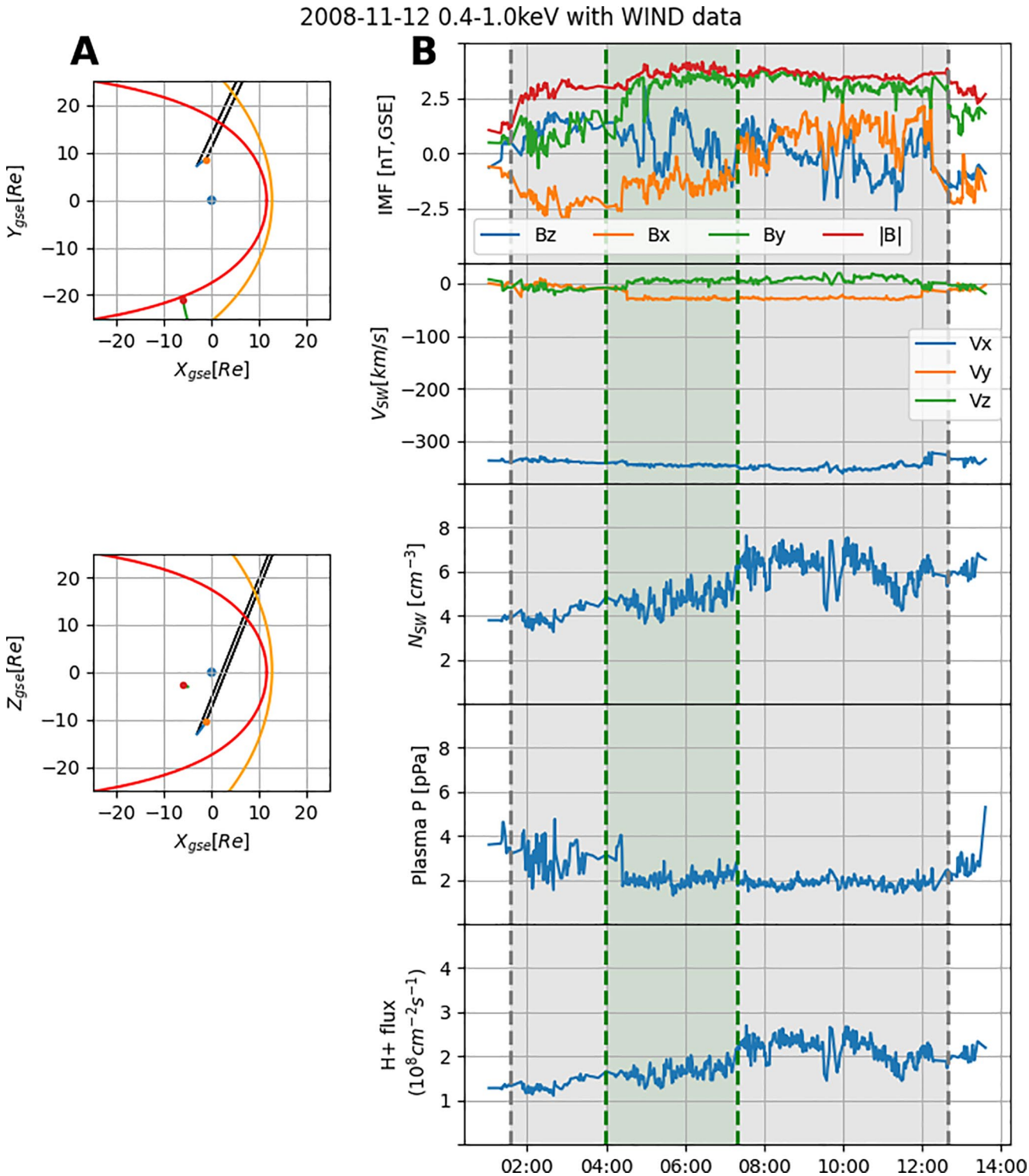

Figure 3. (a) X-ray Multimirror Mission (XMM) orbit (blue), its line of sight (LOS) direction (black), and the THEMIS B orbit (green) projected on the Geocentric Solar Ecliptic (GSE) XY (top) and XZ (bottom) planes. The starting location of XMM and THEMIS B are shown as orange and red dots, respectively. The yellow and red curves show the bow shock (Jeřáb et al., 2005) and the magnetopause (Shue et al., 1998), respectively (b) Solar wind and interplanetary magnetic field (IMF) conditions during the XMM observation (green area) and during the THEMIS B magnetosheath crossing (gray area), obtained from WIND. The IMF, solar wind velocity, number density, plasma pressure (=nkT), and solar wind proton flux ($=n_{sw}v_{sw}$) in the GSE coordinates are shown from top to bottom.

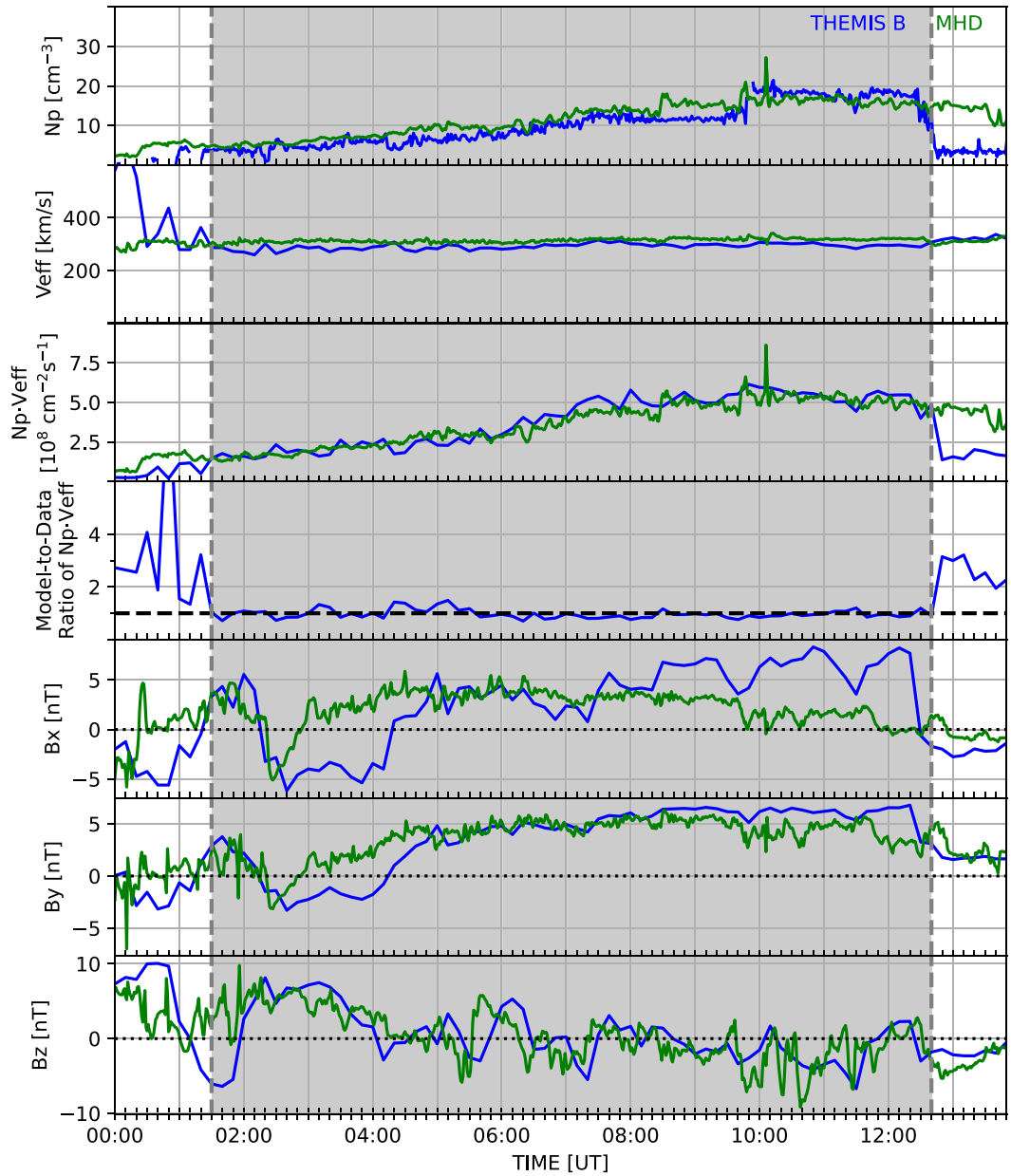

Figure 4. Comparison of the OpenGGCM results (green) with the THEMIS B plasma observation (blue) on 12 November 2008. From top to bottom, the plasma density, effective plasma velocity, effective flux, model-to-data ratio of the effective flux, and three magnetic field components (Bx, By, Bz) are shown. The gray shaded area indicates when the THEMIS B passed through the magnetosheath. The dashed black line in the plot of the model-to-data ratio of the effective flux shows where the model-to-data ratio equals 1.

Figure 4 compares the OpenGGCM data (green) with the THEMIS B observations (blue). The plasma density (N_p), effective velocity (V_{eff}), effective flux ($N_p \times v_{eff}$), model-to-data ratio of the effective flux, and three magnetic field components (Bx, By, Bz) are shown from top to bottom. The model-to-data comparison of the effective flux ($N_p \times v_{eff}$) is shown because this flux is a key parameter that determines potential reaction rates (Q) and thus, contributes to the estimation of the characteristic neutral density (N_0), as seen in Equations 5 and 10. While THEMIS B crosses the magnetosheath (the gray shaded area), the model-to-data ratio is nearly 1, which suggests that the MHD model reasonably reproduced the magnetosheath plasma conditions. The modeled By and Bz components show good agreement with the THEMIS observations, while the Bx component shows a larger discrepancy with the data. However, this model-data gap in Bx is expected because MHD models (not only

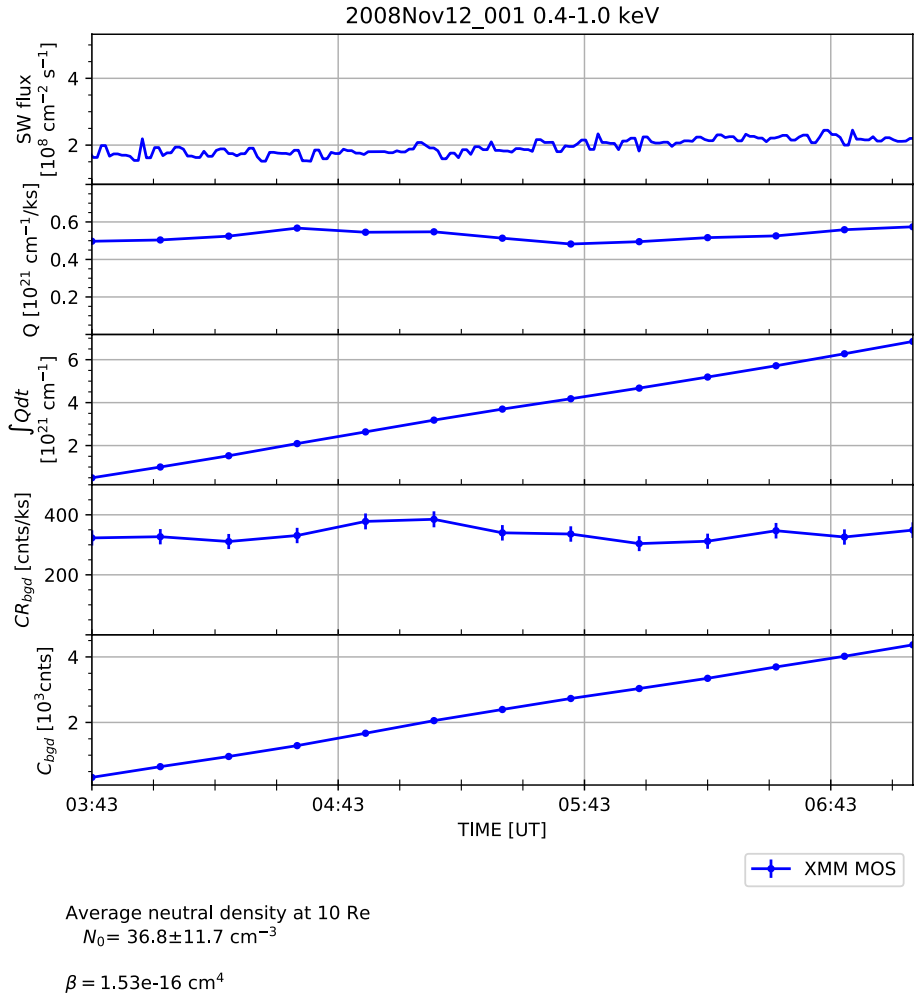

Figure 5. Modeled potential reaction rate and total XMM background counts of the 12 November 2008 event. From top to bottom, the solar wind flux, modeled potential reaction rate (Q), accumulated potential reaction rate ($\int Qdt$), total XMM background count rate (CR_{bgd}), and accumulated XMM count rates ($\int C_{bgd}$) are shown. The effective scale factor β is shown at the bottom of the figure.

OpenGGCM but also other MHD models) often set the IMF Bx at a constant value or put constraints on Bx to save IMF By and Bz in the model input (Raeder et al., 2008), due to the lack of the community's knowledge on the 3D structure of the solar wind/IMF conditions. This magnetic field discrepancy did not affect our calculation of the soft X-ray emission, since the soft X-ray depends on the magnetosheath proton flux whose model-to-data ratio is almost 1.

Figure 5 presents solar wind flux, modeled potential reaction rate (Q), accumulated potential reaction rate ($\int Qdt$), XMM-background count rate (C_{bgd}), and accumulated XMM background counts ($\int C_{bgd}dt$) from top to bottom. C_{bgd} is the total XMM background counts after the astrophysical point source removal, including not only the near-Earth SWCX signal but also the astronomical, heliospheric, and particle background. A fluctuation in C_{bgd} can be considered due to the near-Earth SWCX variation because other background counts vary in a much longer time scale than the ~3.3 hr of our observation period. Solar wind flux is nearly constant during this event, as are the modeled potential reaction rate and the XMM background counts.

The total near-Earth SWCX count on the 12 November 2008 event is 102, very weak compared to the count rates in CC2019 that went up to 250 counts/ks. To increase the source-to-noise ratio of the XMM data, we used the total accumulated potential reaction rate ($\int Qdt$) and the total near-Earth SWCX (C_{SWCX}) during the 3.3-hr event.

From Equation 10, we obtained an exospheric density near the subsolar magnetopause at 36.8 cm^{-3}. Here, we used the count and the accumulated potential reaction rate instead of the count rate and the potential reaction rate.

5.3. Error Analysis

We calculated the uncertainty of the neutral density measurement by estimating and propagating the error in the near-Earth XMM counts (C_{SWCX}) obtained from the soft X-ray background removal process and the error in the potential reaction rate (Q) from the model-data magnetosheath boundary mismatch.

As described in Section 5.1, we obtained C_{SWCX} by subtracting the instrumental background (C_{inst}), sky background (C_{sky}), and heliospheric background (C_{helio}) from the total XMM background counts (C_{bgd}).

$$C_{SWCX} = C_{bgd} - C_{inst} - C_{sky} - C_{helio} \tag{11}$$

We calculated the error in C_{SWCX} by propagating Poisson errors in each component:

$$E_{SWCX} = \sqrt{E_{bgd}^2 + E_{inst}^2 + E_{sky}^2 + E_{helio}^2} \tag{12}$$

We estimated the relative error (E_{SWCX}/C_{SWCX}) for the 12 November 2008 event at 18%.

The soft X-ray emission of this event mostly comes from the magnetosheath (see the XMM LOS in Figure 3a), and therefore depends on the magnetosheath plasma flux and the magnetosheath thickness along the LOS. The model-data comparison in Figure 4 shows that OpenGGCM reasonably reproduces the magnetosheath plasma flux. However, OpenGGCM shows a wider magnetosheath than the THEMIS observation. During this event, THEMIS B observes multiple magnetopause crossings, from 00:30 UT until it fully enters the magnetosheath at 01:30 UT. At ~12:40 UT, THEMIS crosses the bow shock and enters the upstream solar wind. However, the simulated spacecraft in OpenGGCM crosses the magnetopause around 00:20 UT, earlier than THEMIS B does, and stays still in the magnetosheath at 12:40 UT when THEMIS B went out to the solar wind. OpenGGCM provides an approximate calculation of the Earth's magnetospheric system under a single-fluid MHD theory, so it is understandable if it does not reproduce all the magnetopause crossings observed in THEMIS B. The temporary motion of the magnetosheath boundaries does not significantly affect the calculation of Q because such impact is smoothed out during the 3-hr observations of the soft X-ray emission. The important factor is whether our model can catch the average magnetosheath boundaries correctly. The model-data comparison in Figure 4 shows a thicker magnetosheath than that in the THEMIS B observations. This thicker magnetosheath in the MHD model over-estimates Q due to its longer integration path, and subsequently underestimates exosphere density (N_0) in Equation 10. The error in the estimate of Q caused by the model-data boundary mismatch must be addressed. However, due to the limited number of satellites, it is difficult to know the three-dimensional locations of the magnetopause and the bow shock for the entire observation period.

We calculated the maximum error in Q while assuming that the difference between the modeled and observed boundaries was constant throughout the observation period. We used the THEMIS magnetopause and bow shock crossings at 01:34 and 12:40 UT, respectively, as our reference points when we calculated the distances between the modeled and observed boundaries. Then, we shifted the modeled magnetopause sunward and the modeled bow shock earthward according to their boundary difference, and we obtained the narrowest possible magnetosheath during the observation period. Finally, we obtained Q from the narrowest magnetosheath and calculate the relative difference between the Qs from the unmodified and modified magnetosheath as the maximum possible error in Q. The resulting maximum error in Q is 23%.

By propagating 23% of the Q error and 18% of the C_{SWCX} error, we obtained 29% of the neutral density error. The resulting neutral density and its error were estimated at 36.8 $\pm$ 11.7 cm^{-3}. Note that the characteristic exospheric density (N_0) estimated from the 12 November 2008 event is likely to be a lower-limit value. First, the sky background obtained from the ROSAT data (C_{sky}) might have had a fraction that originated from the heliosphere. This could have led to the over-subtraction of C_{helio} and thus, to underestimation of C_{SWCX} and N_0. Second, β is likely lower than that used in our study, thus underestimating N_0. Due to the severe lack of solar wind heavy ion data, previous studies have shown discrepancies in the high-charge-state ion abundances in the solar wind (Carter et al., 2010; Cravens et al., 2001; Koutroumpa et al., 2006; Pepino et al., 2004; Robertson et al., 2006; Whittaker & Sembay, 2016), which caused difficulties in calculating β. We used Koutroumpa et al. (2006) because it

provided a comprehensive list of high-charge-state ions, and thus, was well suited to our wide-band soft X-ray analysis. However, we found that some ion abundances in Koutroumpa et al. (2006) are larger than those in other studies, which led to a large β. Finally, the overestimation of the potential reaction rate (Q) in the MHD model is supposed to create only a positive error. However, the error analysis used in our study naturally assumed that both positive and negative errors are possible in Q. We emphasize the upper error bar more than the lower error bar in our interpretation of our density estimate. In conclusion, our neutral density estimates can be considered lower-limit estimates at the $10R_E$ subsolar location. The actual density is likely to be larger than 36.8 cm^{-3}.

6. Discussion

The exospheric density above the $8R_E$ geocentric distance and its variation during a solar cycle are poorly understood due to severe lack of geocoronal data. CC2019 and Fuselier et al. (2010); Fuselier et al. (2020) showed that from the XMM soft X-ray observations and the IBEX ENA observations of the Earth's magnetosheath it is possible to derive the exospheric density at the $10R_E$ subsolar location, that is, a typical location of the subsolar magnetopause. Their density estimates range from 4 to 58 cm^{-3}, with the lowest end coming from the IBEX data (Fuselier et al., 2010) and the highest end from the XMM data (Connor & Carter, 2019). CC2019 considered the solar cycle a possible reason for this large discrepancy as they pointed out that the IBEX cases in Fuselier et al. (2010) occurred during solar minimum, whereas the XMM cases in CC2019 occurred near solar maximum. However, Fuselier et al. (2020) derived a solar maximum neutral density of 11–18 cm^{-3} from an IBEX event on 4 November 2015, that was not very different from the solar minimum density of 4–11 cm^{-3} from five IBEX events in 2008 and 2009. They concluded that the dayside outer exosphere is weakly dependent on the solar cycle, although they cautiously pointed out that the F10.7 solar irradiance index of their solar maximum event is 110 solar flux units (sfu), lower than the 144.4 sfu and 205.8 sfu of the two solar maximum events of CC2019.

The large density discrepancy between the XMM of our result and that of the IBEX studies still exists, partly due to the inherent difference between the two datasets and partly due to the different density derivation techniques used. For example, the ENA observations are very sensitive to plasma velocity distributions (Connor et al., 2021). For accurate neutral density estimation, a realistic magnetosheath model and sophisticated analysis of the magnetosheath ion flux that moves toward the IBEX detector are necessary. However, the IBEX neutral density studies calculated the magnetosheath ion flux along a simplified IBEX LOS direction by assuming time-independent and homogeneous magnetosheath plasma conditions (Fuselier et al., 2010) or by using a static gas-dynamic magnetosheath model without considering the magnetosheath plasma temperature variation and the full Compton-Getting effect (i.e., the relative motion of the magnetosheath plasma and the IBEX ENA detector; Fuselier et al., 2020), as pointed out in Sibeck et al. (2021). On the other hand, the XMM mission is designed to optimize the signal-to-noise ratio for astrophysical sources with a pencil beam FOV and a long observation time for a specific target. As a result, we had to execute a long background removal process as described in Section 5.1. This observational difficulty will be addressed to some extent by the wide-FOV LEXI and SMILE missions, which will observe the magnetosheath as a main target. Additionally, the abundance of the high-charge-state ions required for the charge exchange process needs to be studied in further detail, highlighting the need for an independent and new space mission with a heavy ion detector, for the most accurate calculation of β and N_0. Our study focused on the lower limit of exospheric neutral density during solar minimum by selecting a large β, to understand the lower limit of the magnetosheath SWCX signals for the SMILE and the LEXI and in an attempt to reduce the large discrepancy between the neutral densities from the XMM and the IBEX studies. We found that our density estimate, 36.8 $\pm$ 11.7 cm^{-3}, are still higher than 4–17 cm^{-3} of Fuselier et al. (2010); Fuselier et al. (2020) but comparable to other geocorona studies, 24–46 cm^{-3} of Zoennchen et al. (2015) and the 41 cm^{-3} of Baliukin et al. (2019), although these geocoronal studies may have had large uncertainties due to their observational difficulties above 8 R_E geocentric distances. Additionally, our exospheric density estimate at 10 R_E subsolar location is higher than the 25 cm^{-3}, adopted by the SMILE modeling working group for the near-Earth SWCX prediction (Branduardi-Raymont et al., 2018).

Although the direct comparison of the XMM and IBEX densities has been troublesome, comparison of XMM observations are still meaningful because it clears some ambiguities caused by the different datasets and the different density derivation techniques. Considering the error bars, our solar minimum neutral density is consistent with the 39.9 $\pm$ 8.0 and 57.6 $\pm$ 8.0 cm^{-3} solar maximum neutral densities from the two CC2019 events. This seems to support a similar conclusion of Fuselier et al. (2020), that is, on the minimal response of the outer

exospheric density to the solar cycle. However, only a handful of XMM events (two for solar maximum and one for solar minimum) and IBEX events (one for solar maximum and five for solar minimum) have been studied so far. More statistical approaches are needed before testing this hypothesis. Our list of potential XMM-SWCX events would be a useful resource for such a statistical analysis. For our future work, we will conduct more case studies using our list and investigate the solar cycle—neutral density relation near the subsolar magnetopause.

7. Summary

The LEXI and SMILE missions will observe the Earth's magnetosheath and cusps through X-ray emissions after their respective launches in 2023 and 2024. Measurements of the near-Earth X-ray signal from these missions will allow the derivation of the neutral density near the subsolar magnetopause, an important parameter in the study of the atmosphere-solar wind interaction. We utilized the magnetosheath soft X-ray observations obtained from the XMM astrophysics mission to calculate a solar minimum exospheric neutral density at the 10 R_E subsolar location, where the subsolar magnetopause is typically located. First, we surveyed ∼11 years of XMM observations, and found 193 potential near-Earth SWCX events that are well suited to our density derivation technique. Second, we estimated the exospheric density from a solar minimum event on 12 November 2008 by improving the density derivation technique of CC2019. From the raw XMM observations, we obtained near-Earth soft X-ray data. Then, we subtracted the magnetosheath plasma contribution from the X-ray signals using the OpenGGCM simulation and derived an exospheric density of 36.8 ± 11.7 cm^{-3} at 10 R_E subsolar location during solar minimum. Due to our potential overestimation of the heliospheric signals (C_{helio}), effective scale factor (β), and potential reaction rate (Q), our density should be considered a lower limit. The actual neutral density is likely to be larger than 36.8 cm^{-3}. Finally, we compared our results with those of previous studies. Our neutral density is within the range of previously reported densities, 4–59 cm^{-3}. Our solar minimum value is consistent with the values at solar maximum of 39.9–57.6 cm^{-3} in CC2019, considering the error bars. This implies that the solar cycle has a minimal impact on the outer exosphere density, as suggested by Fuselier et al. (2020). However, only a handful of event studies had been reported in the literature. Further statistical analysis is needed to conclusively determine the solar cycle—neutral density relation. The neutral density behavior of the outer exosphere will help us understand the Earth's atmospheric loss due to the dynamic space environment and thus, to infer the entire evolutionary history of the Earth's atmosphere as well as of other planetary atmospheres.

Data Availability Statement

WIND SWE and MFI data are available at https://cdaweb.gsfc.nasa.gov/index.html website and potential SWCX event list and OpenGGCM results are available at https://github.com/jjung11/XMM2021. HEASARC tooklit can be found via https://heasarc.gsfc.nasa.gov/ftools/ (we used HEASoft version 6.25), XMM Science Analysis System can be found at https://www.cosmos.esa.int/web/xmm-newton/sas. XMM observations data can be downloaded from http://nxsa.esac.esa.int/nxsa-web/#home. XSPEC is available at https://heasarc.gsfc.nasa.gov/xanadu/xspec/ The effective area of the XMM MOS cameras is documented at https://xmm-tools.cosmos.esa.int/external/xmm_user_support/documentation/uhb/epicfilters.html.

Acknowledgments
This work was supported by the NSF grant AGS-1928883 and the NASA grants, 80NSSC18K1043 and 80NSSC20K1670, and 80MSFC20C0019. Hyunju K. Connor gratefully acknowledges support from the NSF grant OIA-1920965 and the NASA grants, 80NSSC18K1042 and 80NSSC19K0844. We also acknowledge the support from the International Space Science Institute on the ISSI time 492, "title the Earth's Exosphere and its Response to Space Weather". We appreciate Jochen Zoennchen at Argelander Institut für Astronomie, and Igor Baliukin at Space Research Institute for useful discussions on the X-ray background signals. Dimitra Koutrompa's heliospheric SWCX modeling work was supported by CNES and performed with the High Performance Computer and Visualisation platform (HPCaVe) hosted by UPMC-Sorbonne Universités. Jennifer Alyson Carter gratefully acknowledges support from the UK Science Technology Facilities Council (STFC) consolidated grant ST/S000429/1.

References

Auster, H., Glassmeier, K., Magnes, W., Aydogar, O., Baumjohann, W., Constantinescu, D., et al. (2008). The themis fluxgate magnetometer. *Space Science Reviews*, *141*(1–4), 235–264. https://doi.org/10.1007/s11214-008-9365-9

Bailey, J., & Gruntman, M. (2011). Experimental study of exospheric hydrogen atom distributions by Lyman-alpha detectors on the twins mission. *Journal of Geophysical Research*, *116*(A9). https://doi.org/10.1029/2011ja016531

Baliukin, I. I., Bertaux, J.-L., Quémerais, E., Izmodenov, V., & Schmidt, W. (2019). SWAN/SOHO Lyman-α mapping: The hydrogen geocorona extends well beyond the moon. *Journal of Geophysical Research: Space Physics*, *124*(2), 861–885. https://doi.org/10.1029/2018ja026136

Branduardi-Raymont, G., Wang, C., Dai, L., Donovan, E., Li, L., & Sembay, S. (2018). *Smile definition study report*. ESA/SCI.1.

Bzowski, M., Sokol, J., Tokumaru, M., Fujiki, K., Quemerais, E., Lallement, R., & McComas, D. (2013). Solar parameters for modeling interplanetary background, chapter 3. In *Cross-calibration of past and present far UV spectra of solar system objects and the heliosphere* (Tech. Rep.). ISSI Scientific Report.

Carter, J., & Sembay, S. (2008). Identifying XMM-Newton observations affected by solar wind charge exchange. Part i. *Astronomy & Astrophysics*, *489*(2), 837–848. https://doi.org/10.1051/0004-6361:200809997

Carter, J., Sembay, S., & Read, A. (2010). A high charge state coronal mass ejection seen through solar wind charge exchange emission as detected by XMM-Newton. *Monthly Notices of the Royal Astronomical Society*, *402*(2), 867–878. https://doi.org/10.1111/j.1365-2966.2009.15985.x

Carter, J., Sembay, S., & Read, A. (2011). Identifying XMM-Newton observations affected by solar wind charge exchange–Part ii. *Astronomy & Astrophysics*, *527*, A115. https://doi.org/10.1051/0004-6361/201015817

Connor, H., & Carter, J. A. (2019). Exospheric neutral hydrogen density at the nominal 10 re subsolar point deduced from XMM-Newton X-ray observations. *Journal of Geophysical Research: Space Physics*, *124*(3), 1612–1624. https://doi.org/10.1029/2018ja026187

Connor, H., Raeder, J., Sibeck, D., & Trattner, K. (2015). Relation between cusp ion structures and dayside reconnection for four IMF clock angles: OpenGGCM-LTPT results. *Journal of Geophysical Research: Space Physics*, *120*(6), 4890–4906. https://doi.org/10.1002/2015ja021156

Connor, H., Raeder, J., & Trattner, K. (2012). Dynamic modeling of cusp ion structures. *Journal of Geophysical Research*, *117*(A4). https://doi.org/10.1029/2011ja017203

Connor, H., Sibeck, D., Collier, M., Baliukin, I., Branduardi-Raymont, G., Brandt, P., et al. (2021). Soft X-ray and ENA imaging of the earth's dayside magnetosphere. *Journal of geophysical research. Space physics*, *126*(3). https://doi.org/10.1029/2020ja028816

Connor, H., Zesta, E., Fedrizzi, M., Shi, Y., Raeder, J., Codrescu, M. V., & Fuller-Rowell, T. J. (2016). Modeling the ionosphere-thermosphere response to a geomagnetic storm using physics-based magnetospheric energy input: OpenGGCM-CTIM results. *Journal of Space Weather and Space Climate*, *6*, A25. https://doi.org/10.1051/swsc/2016019

Connor, H., Zesta, E., Ober, D., & Raeder, J. (2014). The relation between transpolar potential and reconnection rates during sudden enhancement of solar wind dynamic pressure: OpenGGCM-CTIM results. *Journal of Geophysical Research*, *119*(5), 3411–3429. https://doi.org/10.1002/2013ja019728

Cramer, W. D., Raeder, J., Toffoletto, F., Gilson, M., & Hu, B. (2017). Plasma sheet injections into the inner magnetosphere: Two-way coupled openGGCM-RCM model results. *Journal of Geophysical Research: Space Physics*, *122*(5), 5077–5091. https://doi.org/10.1002/2017ja024104

Cravens, T. (1997). Comet hyakutake X-ray source: Charge transfer of solar wind heavy ions. *Geophysical Research Letters*, *24*(1), 105–108. https://doi.org/10.1029/96gl03780

Cravens, T., Robertson, I., & Snowden, S. (2001). Temporal variations of geocoronal and heliospheric X-ray emission associated with the solar wind interaction with neutrals. *Journal of Geophysical Research: Space Physics*, *106*(A11), 24883–24892. https://doi.org/10.1029/2000ja000461

Dalaudier, F., Bertaux, J., Kurt, V., & Mironova, E. (1984). Characteristics of interstellar helium observed with prognoz 6 58.4-nm photometers. *Astronomy and Astrophysics*, *134*, 171–184.

de la Calle, I. (2021). *Users guide of the XMM-Newton science analysis system*. Issue 16.0, 2021. (ESAXMM-Newton SOC).

De Luca, A., & Molendi, S. (2004). The 2–8 kev cosmic X-ray background spectrum as observed with XMM-Newton. *Astronomy & Astrophysics*, *419*(3), 837–848. https://doi.org/10.1051/0004-6361:20034421

Dimmock, A., & Nykyri, K. (2013). The statistical mapping of magnetosheath plasma properties based on THEMIS measurements in the magnetosheath interplanetary medium reference frame. *Journal of Geophysical Research: Space Physics*, *118*(8), 4963–4976. https://doi.org/10.1002/jgra.50465

Ferdousi, B., & Raeder, J. (2016). Signal propagation time from the magnetotail to the ionosphere: OpenGGCM simulation. *Journal of Geophysical Research: Space Physics*, *121*(7), 6549–6561. https://doi.org/10.1002/2016ja022445

Ferdousi, B., Raeder, J., Zesta, E., Cramer, W., & Murphy, K. (2021). Association of auroral streamers and bursty bulk flows during different states of the magnetotail: A case study. *Journal of Geophysical Research: Space Physics*, *126*(9), e2021JA029329. https://doi.org/10.1029/2021ja029329

Funsten, H., Allegrini, F., Bochsler, P., Dunn, G., Ellis, S., Everett, D., et al. (2009). The interstellar boundary explorer high energy (IBEX-HI) neutral atom imager. *Space Science Reviews*, *146*(1–4), 75–103. https://doi.org/10.1007/978-1-4419-1448-4_5

Fuselier, S., Bochsler, P., Chornay, D., Clark, G., Crew, G., Dunn, G., et al. (2009). The IBEX-Lo sensor. *Space Science Reviews*, *146*(1–4), 117–147. https://doi.org/10.1007/978-1-4419-1448-4_7

Fuselier, S., Dayeh, M., Galli, A., Funsten, H., Schwadron, N., Petrinec, S., et al. (2020). Neutral atom imaging of the solar wind-magnetosphere-exosphere interaction near the subsolar magnetopause. *Geophysical Research Letters*, *47*(19), e2020GL089362. https://doi.org/10.1029/2020gl089362

Fuselier, S., Funsten, H., Heirtzler, D., Janzen, P., Kucharek, H., McComas, D., et al. (2010). Energetic neutral atoms from the earth's subsolar magnetopause. *Geophysical Research Letters*, *37*(13). https://doi.org/10.1029/2010gl044140

Galeazzi, M., Gupta, A., Covey, K., & Ursino, E. (2007). XMM-Newton observations of the diffuse X-ray background. *The Astrophysical Journal*, *658*(2), 1081–1087. https://doi.org/10.1086/512032

Ishikawa, K., Ezoe, Y., Miyoshi, Y., Terada, N., Mitsuda, K., & Ohashi, T. (2013). Suzaku observation of strong solar-wind charge-exchange emission from the terrestrial exosphere during a geomagnetic storm. *Publications of the Astronomical Society of Japan*, *65*(3). https://doi.org/10.1093/pasj/65.3.63

Jansen, F., Lumb, D., Altieri, B., Clavel, J., Ehle, M., Erd, C., et al. (2001). XMM-Newton observatory-i. The spacecraft and operations. *Astronomy & Astrophysics*, *365*(1), L1–L6. https://doi.org/10.1051/0004-6361:20000036

Jensen, J. B., Raeder, J., Maynard, K., & Cramer, W. D. (2017). Particle precipitation effects on convection and the magnetic reconnection rate in earth's magnetosphere. *Journal of Geophysical Research: Space Physics*, *122*(11), 11–413. https://doi.org/10.1002/2017ja024030

Jeřáb, M., Němeček, Z., Šafránková, J., Jelínek, K., & Měrka, J. (2005). Improved bow shock model with dependence on the IMF strength. *Planetary and Space Science*, *53*(1–3), 85–93.

Kavosi, S., Spence, H., Fennell, J., Turner, D., Connor, H., & Raeder, J. (2018). Mms/feeps observations of electron microinjections due to Kelvin–Helmholtz waves and flux transfer events: A case study. *Journal of Geophysical Research: Space Physics*, *123*(7), 5364–5378. https://doi.org/10.1029/2018ja025244

Kivelson, M. G., & Bagenal, F. (2014). Planetary magnetospheres. In *Encyclopedia of the solar system* (pp. 137–157). Elsevier. https://doi.org/10.1016/b978-0-12-415845-0.00007-4

Koutroumpa, D., Lallement, R., Kharchenko, V., Dalgarno, A., Pepino, R., Izmodenov, V., & Quémerais, E. (2006). Charge-transfer induced EUV and soft X-ray emissions in the heliosphere. *Astronomy & Astrophysics*, *460*(1), 289–300. https://doi.org/10.1051/0004-6361:20065250

Koutroumpa, D., Quémerais, E., Ferron, S., & Schmidt, W. (2019). Global distribution of the solar wind flux and velocity from SOHO/SWAN during sc-23 and sc-24. *Geophysical Research Letters*, *46*(8), 4114–4121. https://doi.org/10.1029/2019gl082402

Kuntz, K. D. (2019). Solar wind charge exchange: An astrophysical nuisance. *Astronomy and Astrophysics Review*, *27*(1), 1–71. https://doi.org/10.1007/s00159-018-0114-0

Kuntz, K. D., Collado-Vega, Y., Collier, M. R., Connor, H., Cravens, T. E., Koutroumpa, D., et al. (2015). The solar wind charge-exchange production factor for hydrogen. *The Astrophysical Journal*, *808*(2), 143. https://doi.org/10.1088/0004-637x/808/2/143

Kuntz, K. D., & Snowden, S. (2008). The EPIC-MOS particle-induced background spectra. *Astronomy & Astrophysics*, *478*(2), 575–596. https://doi.org/10.1051/0004-6361:20077912

Lallement, R., Bertaux, J., & Dalaudier, F. (1985). Interplanetary Lyman-alpha spectral profiles and intensities for both repulsive and attractive solar force fields predicted absorption pattern by a hydrogen cell. *Astronomy and Astrophysics*, *150*, 21–32.

Lepping, R., Acũna, M., Burlaga, L., Farrell, W., Slavin, J., Schatten, K., et al. (1995). The wind magnetic field investigation. *Space Science Reviews*, *71*(1–4), 207–229. https://doi.org/10.1007/bf00751330

Lisse, C., Dennerl, K., Englhauser, J., Harden, M., Marshall, F., Mumma, M., et al. (1996). Discovery of X-ray and extreme ultraviolet emission from comet c/hyakutake 1996 b2. *Science*, *274*(5285), 205–209. https://doi.org/10.1126/science.274.5285.205

Lumb, D., Warwick, R., Page, M., & De Luca, A. (2002). X-ray background measurements with XMM-Newton EPIC. *Astronomy & Astrophysics*, *389*(1), 93–105. https://doi.org/10.1051/0004-6361:20020531

Machol, J., Snow, M., Woodraska, D., Woods, T., Viereck, R., & Coddington, O. (2019). An improved Lyman-alpha composite. *Earth and Space Science*, *6*(12), 2263–2272. https://doi.org/10.1029/2019ea000648

McComas, D., Allegrini, F., Bochsler, P., Bzowski, M., Collier, M., Fahr, H., et al. (2009). IBEX—Interstellar boundary explorer. *Space Science Reviews*, *146*(1), 11–33. https://doi.org/10.1007/978-1-4419-1448-4_3

McFadden, J., Carlson, C., Larson, D., Ludlam, M., Abiad, R., Elliott, B., & Angelopoulos, V. (2008). The THEMIS ESA plasma instrument and in-flight calibration. *Space Science Reviews*, *141*(1), 277–302. https://doi.org/10.1007/s11214-008-9440-2

McMullin, D., Bzowski, M., Möbius, E., Pauluhn, A., Skoug, R., Thompson, W., et al. (2004). Heliospheric conditions that affect the interstellar gas inside the heliosphere. *Astronomy & Astrophysics*, *426*(3), 885–895. https://doi.org/10.1051/0004-6361:20047147

Mitsuda, K., Bautz, M., Inoue, H., Kelley, R. L., Koyama, K., Kunieda, H., et al. (2007). The X-ray observatory Suzaku. *Publications of the Astronomical Society of Japan*, *59*(sp1), S1–S7.

Morrison, R., & McCammon, D. (1983). Interstellar photoelectric absorption cross sections, 0.03–10 kev. *The Astrophysical Journal*, *270*, 119–122. https://doi.org/10.1086/161102

Ogilvie, K., Chornay, D., Fritzenreiter, R., Hunsaker, F., Keller, J., Lobell, J., et al. (1995). SWE, a comprehensive plasma instrument for the wind spacecraft. *Space Science Reviews*, *71*(1), 55–77. https://doi.org/10.1007/bf00751326

Oliveira, D. M., & Raeder, J. (2015). Impact angle control of interplanetary shock geoeffectiveness: A statistical study. *Journal of Geophysical Research: Space Physics*, *120*(6), 4313–4323. https://doi.org/10.1002/2015ja021147

Østgaard, N., Mende, S., Frey, H., Gladstone, G., & Lauche, H. (2003). Neutral hydrogen density profiles derived from geocoronal imaging. *Journal of Geophysical Research*, *108*(A7). https://doi.org/10.1029/2002ja009749

Pepino, R., Kharchenko, V., Dalgarno, A., & Lallement, R. (2004). Spectra of the X-ray emission induced in the interaction between the solar wind and the heliospheric gas. *The Astrophysical Journal*, *617*(2), 1347–1352. https://doi.org/10.1086/425682

Raeder, J., Larson, D., Li, W., Kepko, E. L., & Fuller-Rowell, T. (2008). OpenGGCM simulations for the THEMIS mission. *Space Science Reviews*, *141*(1), 535–555. https://doi.org/10.1007/s11214-008-9421-5

Raeder, J., McPherron, R., Frank, L., Kokubun, S., Lu, G., Mukai, T., et al. (2001). Global simulation of the geospace environment modeling substorm challenge event. *Journal of Geophysical Research: Space Physics*, *106*(A1), 381–395. https://doi.org/10.1029/2000ja000605

Robertson, I., Collier, M., Cravens, T., & Fok, M.-C. (2006). X-ray emission from the terrestrial magnetosheath including the cusps. *Journal of Geophysical Research*, *111*(A12). https://doi.org/10.1029/2006ja011672

Shi, Y., Zesta, E., Connor, H., Su, Y.-J., Sutton, E., Huang, C., & Oliveira, D. (2017). High-latitude thermosphere neutral density response to solar wind dynamic pressure enhancement. *Journal of Geophysical Research: Space Physics*, *122*(11), 11–559. https://doi.org/10.1002/2017ja023889

Shue, J.-H., Song, P., Russell, C., Steinberg, J., Chao, J., Zastenker, G., et al. (1998). Magnetopause location under extreme solar wind conditions. *Journal of Geophysical Research*, *103*(A8), 17691–17700. https://doi.org/10.1029/98ja01103

Sibeck, D. G., Allen, R., Aryan, H., Bodewits, D., Brandt, P., Branduardi-Raymont, G., et al. (2018). Imaging plasma density structures in the soft X-rays generated by solar wind charge exchange with neutrals. *Space Science Reviews*, *214*(4), 1–124. https://doi.org/10.1007/s11214-018-0504-7

Sibeck, D. G., Collier, M., & Silveira, M. (2021). Neutral densities in the outer exosphere near the subsolar magnetopause. *Geophysical Research Letters*, e2021GL093383. https://doi.org/10.1029/2021gl093383

Smith, R. K., Brickhouse, N. S., Liedahl, D. A., & Raymond, J. C. (2001). Collisional plasma models with APEC/APED: Emission-line diagnostics of hydrogen-like and helium-like ions. *The Astrophysical Journal Letters*, *556*(2), L91–L95. https://doi.org/10.1086/322992

Snowden, S., Egger, R., Freyberg, M., McCammon, D., Plucinsky, P., Sanders, W., et al. (1997). Rosat survey diffuse X-ray background maps. ii. *The Astrophysical Journal*, *485*(1), 125–135. https://doi.org/10.1086/304399

Strüder, L., Briel, U., Dennerl, K., Hartmann, R., Kendziorra, E., Meidinger, N., et al. (2001). The European photon imaging camera on XMM-Newton: The pn-CCD camera. *Astronomy & Astrophysics*, *365*(1), L18–L26. https://doi.org/10.1051/0004-6361:20000066

Turner, M. J., Abbey, A., Arnaud, M., Balasini, M., Barbera, M., Belsole, E., et al. (2001). The European photon imaging camera on XMM-Newton: The MOS cameras. *Astronomy & Astrophysics*, *365*(1), L27–L35. https://doi.org/10.1051/0004-6361:20000087

Walsh, B., Kuntz, K., Collier, M., Sibeck, D., Snowden, S., & Thomas, N. (2014). Energetic particle impact on X-ray imaging with XMM-Newton. *Space Weather*, *12*(6), 387–394. https://doi.org/10.1002/2014sw001046

Weisskopf, M. C., Tananbaum, H. D., Van Speybroeck, L. P., & O'Dell, S. L. (2000). Chandra X-ray observatory (CXO): Overview. In *X-ray optics, instruments, and missions iii* (Vol. 4012, pp. 2–16).

Whittaker, I. C., & Sembay, S. (2016). A comparison of empirical and experimental O^{7+}, O^{8+}, and O/H values, with applications to terrestrial solar wind charge exchange. *Geophysical Research Letters*, *43*(14), 7328–7337. https://doi.org/10.1002/2016gl069914

Whittaker, I. C., Sembay, S., Carter, J. A., Read, A. M., Milan, S. E., & Palmroth, M. (2016). Modeling the magnetospheric X-ray emission from solar wind charge exchange with verification from XMM-Newton observations. *Journal of Geophysical Research: Space Physics*, *121*(5), 4158–4179. https://doi.org/10.1002/2015ja022292

Zoennchen, J., Bailey, J., Nass, U., Gruntman, M., Fahr, H., & Goldstein, J. (2011). The twins exospheric neutral H-density distribution under solar minimum conditions. *Annales geophysicae*, *29*, 2211–2217. https://doi.org/10.5194/angeo-29-2211-2011

Zoennchen, J., Nass, U., & Fahr, H. (2013). Exospheric hydrogen density distributions for equinox and summer solstice observed with twins1/2 during solar minimum. *Annales geophysicae*, *31*, 513–527. https://doi.org/10.5194/angeo-31-513-2013

Zoennchen, J., Nass, U., & Fahr, H. (2015). Terrestrial exospheric hydrogen density distributions under solar minimum and solar maximum conditions observed by the twins stereo mission. *Annales geophysicae*, *33*, 413–426. https://doi.org/10.5194/angeo-33-413-2015

Zoennchen, J., Nass, U., Fahr, H. J., & Goldstein, J. (2017). The response of the H geocorona between 3 and 8 Re to geomagnetic disturbances studied using twins stereo Lyman-α data. *Annales geophysicae*, *35*, 171–179. https://doi.org/10.5194/angeo-35-171-2017